

New method to determine equivalent black carbon mass size distribution

Weilun Zhao¹, Gang Zhao², Ying Li^{3,4}, Song Guo², Nan Ma⁵, Lizi Tang², Zirui Zhang², Chunsheng Zhao¹

¹Department of Atmospheric and Oceanic Sciences, School of Physics, Peking University, Beijing 100871, China

²State Key Joint Laboratory of Environmental Simulation and Pollution Control, College of Environmental Sciences and Engineering, Peking University, Beijing 100871, China

³Department of Ocean Science and Engineering, Southern University of Science and Technology, Shenzhen 518055, China

⁴Southern Marine Science and Engineering Guangdong Laboratory, Guangzhou 511458, China

⁵Institute for Environmental and Climate Research, Jinan University, Guangzhou 511443, China

Correspondence to: Chunsheng Zhao (zcs@pku.edu.cn)

Abstract. Black carbon (BC) is an important atmospheric component with strong light absorption. Many attempts have been made to measure BC mass size distribution (BCMSD) for its significant impact on climate and public health. Larger-coverage BCMSD, ranging from upper submicron to larger than 1 μm , contributes to substantial proportion of total BC mass and absorption. However, current time resolution of larger-coverage BCMSD measurement was limited to 1 day, which was insufficient to characterize variation of larger-coverage BCMSD. In this study, a new method to determine equivalent BCMSD (eBCMSD) was proposed from size-resolved absorption coefficient measured by an aerodynamic aerosol classifier in tandem with an aethalometer. The proposed method could measure larger-coverage eBCMSD with time resolution as high as 1 hour and was validated by comparing the measurement results with ~~that~~ refractory BCMSD (rBCMSD) measured by a differential mobility analyzer in tandem with a single particle soot photometer (DMA – SP2) for particle size larger than 300 nm during a field measurement in Yangtze River Delta. Bulk refractory BC mass concentration ($m_{\text{BC,bulk}}$ / ~~$m_{\text{BC,bulk}}$~~) by DMA – SP2 was underestimated by 33 % compared to ~~that~~ bulk equivalent BC mass concentration ($m_{\text{eBC,bulk}}$) by this method because of the limited size range of measurement for DMA – SP2. Uncertainty analysis of this method was performed with respect to mass absorption cross-section (MAC), transfer function inversion, number fraction of BC-containing particle and instrumental noise. The results indicated that MAC was the main uncertainty source, leading to $m_{\text{eBC,bulk}}$ varied from – 20 % to 28 %. With the advantage of wide size coverage up to 1.5 μm , high time resolution, easy operation and low cost, this method is expected to have wide applications in field measurement for better estimating radiative properties and climate effects of BC.

1 Introduction

Atmospheric black carbon (BC) is emitted through incomplete combustion of carbon-based fuels (Bond, 2001), such as biomass burning and fossil fuel combustion (Bond et al., 2004). BC warms atmosphere and is considered the third important light absorber in the climate system after CO_2 and CH_4 (Bond et al., 2013). BC can induce the respiratory and cardiovascular disease through inhalation (Highwood and Kinnersley, 2006). Plenty of studies have been devoted to BC for its significant impact on the climate and public health.

32 Bulk BC mass concentration ($m_{\text{BC,bulk}}$) is one of the essential parameters for modeling because radiative transfer models calculate
33 BC absorption from $m_{\text{BC,bulk}}$ (Bond et al., 2013). A great deal of research has been dedicated to $m_{\text{BC,bulk}}$ measurement for both model
34 assimilation and environmental monitoring (Castagna et al., 2019; Helin et al., 2018; Ran et al., 2016). A recent study indicated that
35 the radiative effect of BC was extremely sensitive to its particle size (Matsui et al., 2018). Zhao et al. (2019) further revealed that
36 the variation of BC mass size distribution (BCMSD), namely size-resolved BC mass concentration ($m_{\text{BC,size-resolved}}$), led to substantial
37 changes in the radiative effect of BC based on field measurement, highlighting the importance of BCMSD on modeling the radiative
38 effect of BC rather than simply $m_{\text{BC,bulk}}$. The size of BC affects the deposition rate of BC to the lung (Highwood and Kinnersley,
39 2006), indicating that BCMSD is closely related to health. In the ambient environment, BCMSD is influenced by emission sources.
40 For instance, BCMSD of fossil fuel combustion differs obviously from that of biomass burning (Schwarz et al., 2008), implying
41 that BCMSD is one of the characteristics of emission source. The temporal variation of BCMSD can reflect the atmospheric aging
42 of BC, during which BC undergoes remarkable change in size, accompanied by dramatical variation of BC optical properties (Zhang
43 et al., 2008). Therefore, reliable measurement and understanding of BCMSD are highly necessary for estimating the impact of BC
44 on both the earth energy budget and public health (Moosmuller et al., 2009).

45 Quite a few efforts ~~was~~were made to measure BCMSD. The single-particle soot photometer (SP2) was developed using laser-
46 induced incandescence (Schwarz et al., 2006), which measured refractory BCMSD (rBCMSD, Petzold et al. (2013)) on a single-
47 particle level. The soot particle aerosol mass spectrometer (SP-AMS) combined laser-induced incandescence and mass spectroscopy,
48 which could determine not only rBCMSD but also the chemical composition of BC-containing particles (Onasch et al., 2012). The
49 SP2 and SP-AMS techniques were characterized by high time resolution and high accuracy, but high cost and complicated
50 maintenance, as a result, not widely applied for routine measurement. A more convenient solution was required for wider and better
51 characterization of BCMSD in different regions and emission sources. Elemental carbon mass size distribution (ECMSD, Petzold
52 et al. (2013))BCMSD could be sampled by multi-stage cascade impactor (Viidanoja et al., 2002) combined with off-line analysis,
53 such as thermo/optical organic carbon/elemental carbon method (Chow et al., 2001). BCMSD-ECMSD sampled by multi-stage
54 cascade impactor had wide size coverage, but low time resolution, usually from 24 hours (Soto-Garcia et al., 2011) to 48 hours (Guo,
55 2015), which was too low to resolve aging of BC. Differential mobility analyzer (DMA) in tandem with filter-based instrument
56 (Hansen et al., 1984), for instance, micro-aethalometer (MA) (Ning et al., 2013) and particle soot absorption photometer (PSAP)
57 (Tunved et al., 2021), was used to determine equivalent BCMSD (eBCMSD, Petzold et al. (2013)) with higher time resolution up
58 to 2 hours (Zhao et al., 2021b). However, the multiple-charge correction and low flow rate of DMA imposed restrictions on the
59 accuracy of the measured eBCMSD. The measured size range of DMA was limited to less than about 700 nm, resulting in incomplete
60 measured eBCMSD. Current measurement of larger-coverage BCMSD, ranging from upper submicron to larger than 1 μm , was
61 limited in time resolution. Characteristics of larger-coverage BCMSD during atmospheric aging was still unclear. Wang et al. (2022)
62 showed that BC larger than 1 μm could contribute to as large as 50% of $m_{\text{BC,bulk}}$, highlighting the importance of larger-coverage
63 BCMSD. Therefore, it was imperative to measure larger-coverage BCMSD with higher time resolution.

In this study, a new method to determine $eBCMSD$ was proposed using size-resolved absorption coefficient ($\sigma_{ab, size-resolved}$) measured by an aerodynamic aerosol classifier (AAC, Cambustion, UK, Tavakoli and Olfert (2013)) in tandem with an aethalometer (model AE33, Magee, USA, Drinovec et al. (2015)), combined with size-resolved number concentration ($N_{size-resolved}$), simultaneously measured by scanning mobility particle sizer (SMPS, TSI, USA) and an aerodynamic particle sizer (APS, TSI, USA). The proposed method for determining $eBCMSD$ overcame the disadvantages and weighed the advantages of the above-mentioned methods, characterized by high cost-effectiveness, easy and convenient maintenance, high time resolution to 1 hour, and wide size range to up to 1.5 μm . The proposed method was validated in a field measurement in the Yangtze River Delta and the uncertainty study was carried out based on the measured data.

2 Experimental setup Methods

2.1 Instrumental setup

Figure 1 illustrated the instrumental setup developed in this study, which could be split into two parts, namely the measurement setup and the validation setup. Ambient aerosol particles were drawn through a PM_{10} inlet ($16.67 L min^{-1}$) and ambient aerosol particles were dried to relative humidity (RH) less than 30 % by silica gel diffusion drier beforehand. An advanced flow splitter were used to split aerosol laden flow into different instruments for isokinetic sampling. For the measurement setup, AAC in tandem with AE33 (AAC – AE33) measured $\sigma_{ab, size-resolved}$ at a flow rate of $3 L min^{-1}$. Since $eBCMSD$ of larger size coverage was mainly focused in this study, AAC was set to scan 12 logarithmically spaced particle sizes (D_p) logarithmically equally spaced from 200 nm to 1500 nm and smaller size was not scanned. Each size was scanned for 5 minutes and 1 hour was required for a complete cycle. It should be noted that D_p was aerodynamic size in this study. Mobility size related to DMA was converted to aerodynamic size assuming an effective density of $1.3 g cm^{-3}$ (Zhao et al., 2019; DeCarlo et al., 2005). AE33 measured absorption coefficient (σ_{ab}) at 7 wavelengths from 370 nm to 950 nm (Drinovec et al., 2015), at which 880 nm was adopted in this study because BC dominated particle absorption at 880 nm (Ramachandran and Rajesh, 2007). SMPS and APS measured $N_{size-resolved}$ for D_p less than and greater than about 800 nm at a flow rate of $0.3 L min^{-1}$ and $5 L min^{-1}$, respectively.

For validation system, the tandem array of Neutralizer, DMA and SP2 (DMA – SP2) measured $rBCMSD$ ($rBCMSD_{DMA-SP2}$) at a flow rate of $0.12 L min^{-1}$ for purpose of comparing with $eBCMSD$ determined by the proposed method ($eBCMSD_{AAC-AE33}$, $BCMSD_{AAC-AE33}$). The lower detection limit of D_p for DMA – SP2 was about 200 nm. Therefore, lower D_p limit for both $BCMSD_{DMA-SP2}$ and $BCMSD_{AAC-AE33}$ was set as 200 nm in this study. Another AE33 measured bulk absorption coefficient ($\sigma_{ab, bulk}$) simultaneously at a flow rate of $2 L min^{-1}$ for closure study with $\sigma_{ab, size-resolved}$.

2.1.1 Aethalometer model-AE33

The principle of obtaining σ_{ab} was well developed for aethalometer (Hansen et al., 1984) and described here in brief. Ambient aerosol particles were drawn into an aethalometer at a flow rate F and collected on an area S of a filter. A light source illuminated the filter. The transmitted light signal was denoted as $I(I_0)$ for the light which passed through the particle-laden (particle-free) part of the filter. Light attenuation was defined as

$$ATN = -100 \cdot \ln\left(\frac{I}{I_0}\right). \quad (1)$$

ATN increased with decreasing I as aerosol particles were loaded on the filter continuously. Therefore, ATN reflected aerosol loading on the filter. If ATN increased ΔATN during time interval Δt , then attenuation coefficient was defined as

$$\sigma_{ATN} = \frac{S}{100 \cdot F} \cdot \frac{\Delta ATN}{\Delta t}. \quad (2)$$

The light attenuation was caused by not only particle absorption, but also scattering by particle and filter matrix. A scattering parameter C_f was introduced to extract σ_{ab} from σ_{ATN} :

$$\sigma_{ab} = \frac{\sigma_{ATN}}{C_f}, \quad (3)$$

where C_f was set as 2.9 (Zhao et al., 2020b) in this study. Nonlinearity, termed loading effect, became more and more significant with increasing aerosol loading, namely for the same increase in aerosol loading, the corresponding increase in ATN was smaller for heavier aerosol loading. The “dual-spot” technique (Drinovec et al., 2015) was proposed to correct the loading effect for AE33 and was used in this study. The σ_{ab} measured by AE33 at given particle size selected by AAC was termed binned σ_{ab} ($\sigma_{ab, \text{binned}}$) in this study to differentiate from $\sigma_{ab, \text{bulk}}$.

2.3.2.1.2 Aerodynamic aerosol classifier AAC

The principle of AAC was illustrated detailedly by Tavakoli and Olfert (2013) and was introduced here concisely. The setup of AAC could be simplified to two coaxial cylinders, where the inner radius, outer radius and length was denoted as r_i , r_o and L . Polydisperse particles flowed into the space between the inner cylinder and outer cylinder from one end of the inner cylinder at a flow rate of Q_{sample} . Meanwhile, Particle free sheath flow streamed in the space between the inner cylinder and outer cylinder in the direction of the axis of the coaxial cylinders at a flow rate of Q_{sheath} . The sheath flow carried the particles along the coaxial cylinders. At the same time, the two coaxial cylinders rotated with respect to their axis at a rotational speed of ω . Therefore, the particles was migrated outwards across the sheath flow by the centrifugal force acting on them. Relaxation time (τ) was defined as

$$\tau = \frac{C_c(D_p) \rho_0 D_p^2}{18\mu}, \quad (4)$$

where $C_c(D_p)$ was the ~~cunningham-Cunningham~~ Cunningham slip correction factor as a function of D_p (Kim et al., 2005), $\rho_0 = 1 \text{ g cm}^{-3}$ was the reference density and μ was the gas viscosity. It could be seen that τ was directly related to D_p . Dynamic analysis proved that only particles with certain relaxation time τ , and hence certain D_p , could migrate to another end of outer cylinder and emerge as monodisperse flow. τ was related to parameters of AAC by

$$\tau = \frac{2Q_{\text{sheath}}}{\pi\omega^2(r_i+r_o)^2L}. \quad (5)$$

Therefore, by changing ω and Q_{sheath} , monodisperse particles of desired D_p could be selected by AAC. Unlike DMA, particles did not need to be charged before entering AAC. Consequently, the transmission efficiency (λ_Ω) of AAC was about 4 times higher than that of DMA and multi-charge correction was not required for ~~data measured by the instrument downstream AAC~~ AE33 (Johnson et al., 2018).

2.1.3 DMA – SP2

The reason why DMA – SP2 was used rather than SP2 alone was that D_p could be directly measured by DMA. If SP2 was used alone, D_p was calculated from Mie theory with assumed inputs (Taylor et al., 2015). The detail of DMA – SP2 was described by Zhao et al. (2021a) and presented here concisely. The incandescence high gain channel and incandescence low gain channel of SP2 were calibrated by Aquadag soot particles with effective density of 1.8 g cm^{-3} before measurement. DMA was set to scan D_p from 15 nm to 780 nm with 56 bins at time resolution of 5 min. D_p and time resolution of measured rBCMSD_{DMA-SP2} was interpolated and time-averaged to that of eBCMSD_{AAC-AE33} for comparison. It should be noted that 780 nm, the upper D_p limit scanned by DMA, lied between 720 nm and 865 nm, two of the scanned D_p s by AAC. Therefore, upper D_p limit of the interpolated rBCMSD_{DMA-SP2} was 720 nm in this study. Similarly, the lower D_p limit of the interpolated rBCMSD_{DMA-SP2} was 200 nm. According to Zhao et al. (2020a), DMA – SP2 could not detect particle less than about 200 nm, consistent with the lower limit of D_p in this study.

The number distribution of BC-containing particle measured by DMA – SP2 could be presented as a bivariate function $\frac{\partial^2 N_{BC}}{\partial \log D_p \partial \log D_c}$, where N_{BC} was the number concentration of BC-containing particle, and D_c was the core diameter assuming that BC-containing particle had a core-shell geometry. It should be pointed out that asphericity of rBC was not considered in this study. D_c was logarithmically equally distributed from 78 nm to 560 nm with 29 bins. At a given D_c bin, the number distribution of BC-containing particle could be considered as a univariate function $\frac{dN_{BC}}{d \log D_p}$. The multiple charging correction of 1-dimensional size distribution was developed by Knutson and Whitby (1975), which was adopted to correct $\frac{dN_{BC}}{d \log D_p}$. By correcting $\frac{dN_{BC}}{d \log D_p}$ at each D_c bin, multiple charging correction of $\frac{\partial^2 N_{BC}}{\partial \log D_p \partial \log D_c}$ was achieved.

2.5.2 Field measurement

The proposed method was applied to a field measurement in Changzhou, Jiangsu Province, China ($119^\circ 36' \text{E}$, $31^\circ 43' \text{N}$), located in the Yangtze River Delta, from May 17th to June 3rd in 2021. Changzhou was between two megacities, about 187 km to the northwest of Shanghai and about 82 km to the southeast of Nanjing, as shown in Fig. S1a. The area between the Shanghai and Nanjing underwent serious environmental pollution in the past few decades with the development of industrialization and urbanization. As shown in Fig. S1b, the pollution condition of Changzhou was overall representative of the regional background pollution in the Yangtze River Delta.

2.4 Method

2.3 Size-resolved calculations

2.3.1 Deriving size-resolved absorption coefficient from binned absorption coefficient $\sigma_{ab, \text{size-resolved}}$

Tavakoli and Olfert (2013) formulated the ideal theoretical model for AAC transfer function inversion, which was adopted by this study to derive $\sigma_{ab, \text{size-resolved}}$ from $\sigma_{ab, \text{binned}}$ and presented here in short. The $\sigma_{ab, \text{size-resolved}}$ was given by

$$\sigma_{ab, \text{size-resolved}} = \frac{d\sigma_{ab}}{d \log D_p} = \frac{\ln(10)}{d \log D_p} \cdot \beta \cdot \sigma_{ab, \text{binned}} \quad (6)$$

156 where β^* was related to the ratio of Q_{sheath} to Q_{sample} , $R_t = Q_{\text{sheath}}/Q_{\text{sample}} = 1/\beta$, through

$$157 \quad \beta^* = \left(1 + \frac{1}{\beta}\right) \ln(1 + \beta) - \left(1 - \frac{1}{\beta}\right) \ln(1 - \beta). \quad (7)$$

158 Johnson et al. (2018) corrected the ideal inversion formula (6) to take particle loss and spectral broadening into account by replacing

159 β^* with a nonideal β_{NI}^* :

$$160 \quad \beta_{\text{NI}}^* = \lambda_{\Omega} \mu_{\Omega} \left[\ln \left(\frac{1 + \beta/\mu_{\Omega}}{1 + \beta/\mu_{\Omega}} \right) + \frac{\mu_{\Omega}}{\beta} \ln \left(1 - \left(\frac{\mu_{\Omega} \beta}{\beta \mu_{\Omega}} \right)^2 \right) \right], \quad (8)$$

161 where μ_{Ω} was the spectral broadening factor. Both λ_{Ω} and μ_{Ω} were dependent on D_p as well as flow, and discussed in detail in Sect.

162 4.2.

163 **2.4.2 Deriving black carbon mass size distribution from size-resolved absorption coefficient** **2.3.2 eBCMSD_{AAC-AE33}**

164 $\sigma_{\text{ab, size-resolved}}$ could be converted to eBCMSD_{AAC-AE33} through mass absorption cross-section (MAC) (Bond and Bergstrom, 2006);

165 ~~which was assumed a fixed value of 7.77 m²/g for AE33. However, both field measurement and model study manifested that~~

166 ~~MAC varied significantly. A fixed MAC led to uncertainty in derived BCMSD_{AAC-AE33}. In this study, MAC, which~~ was variable

167 ~~determined based on method proposed by Zhao et al. (2021b) for more accurate BCMSD_{AAC-AE33} estimation.~~ Briefly, a 2-

168 dimensional lookup table of MAC with respect to D_p and **BC core diameter (D_c)** was simulated (MAC(D_p , D_c)) by Mie theory

169 assuming a core-shell geometry. At a given size bin centered at D_p , the corresponding σ_{ab} and number concentration (N) at the size

170 bin, denoted as $\sigma_{\text{ab}}(D_p)$ and $N(D_p)$, could be derived by $\sigma_{\text{ab, size-resolved}}$ and $N_{\text{size-resolved}}$:

$$171 \quad \sigma_{\text{ab}}(D_p) = \sigma_{\text{ab, size-resolved}}(D_p) \cdot \Delta \log D_p, \quad (9)$$

$$172 \quad N(D_p) = N_{\text{size-resolved}}(D_p) \cdot \Delta \log D_p, \quad (10)$$

173 where $\Delta \log D_p$ was the logarithmic bin-width of the size bin. The number concentration of BC-containing particle $N_{\text{BC}}(D_p)$ at the

174 size bin $N_{\text{BC}}(D_p)$ was determined by

$$175 \quad N_{\text{BC}}(D_p) = N(D_p) \cdot f_{\text{BC}}, \quad (11)$$

176 where f_{BC} was the number fraction of BC-containing particle, which was assumed as a fixed value in this study and the uncertainty

177 of the fixed- f_{BC} assumption was discussed in Sect. 4.3. An optimal D_c was found so that calculated σ_{ab} at the size bin, denoted as

178 $\sigma_{\text{ab, calc}}(D_p, D_c)$, matched $\sigma_{\text{ab}}(D_p)$:

$$179 \quad \sigma_{\text{ab, calc}}(D_p, D_c) = \rho_{\text{BC}} \frac{\pi}{6} D_c^3 \cdot \text{MAC}(D_p, D_c) \cdot N_{\text{BC}}(D_p) = \sigma_{\text{ab}}(D_p), \quad (12)$$

180 where ρ_{BC} was the density of BC, and set as 1.8 g cm⁻³ (Bond and Bergstrom, 2006), consistent with the ρ_{BC} assumption when

181 deriving rBCMSD_{DMA-SP2}. **Equivalent** BC mass concentration (m_{eBC}) at the size bin, denoted as $m_{\text{eBC}}(D_p)$, could be determined by

$$182 \quad m_{\text{eBC}}(D_p) = \frac{\sigma_{\text{ab}}(D_p)}{\text{MAC}(D_p, D_c)}, \quad (13)$$

183 then the eBCMSD_{AAC-AE33} at D_p , denoted by eBCMSD_{AAC-AE33}(D_p), could be determined by

$$184 \quad \text{eBCMSD}(D_p) = \frac{m_{\text{eBC}}(D_p)}{\Delta \log D_p}. \quad (14)$$

185 **2.5 Field measurement**

The proposed method was applied to a field measurement in Changzhou, Jiangsu Province, China (119°36'E, 31°43'N), located in the Yangtze River Delta, from May 17th to June 3rd in 2021. Changzhou was between two megacities, about 187 km to the northwest of Shanghai and about 82 km to the southeast of Nanjing, as shown in Fig. S1a. The area between the Shanghai and Nanjing underwent serious environmental pollution in the past few decades with the development of industrialization and urbanization. As shown in Fig. S1b, the pollution condition of Changzhou was overall representative of the regional background pollution in the Yangtze River Delta.

3 Results and discussion

Figure 2 presented the time series of the measurement results. There were 4 pollution episodes during the measurement period: from about 12:00 May 18th-17th to about 00:00 May 19th-20th, from about 00:00 May 21st to about 12:00 May 22nd, from about 00:00 May 24th to about 12:00 May 26th, and from about 12:00 May 29th-28th to about 12:00 May 31st, as shown in Fig. 2a. Both $eBCMSD_{AAC-AE33}$ (Fig. 2b) and $rBCMSD_{DMA-SP2}$ (Fig. 2c) recorded the 4 pollution episodes simultaneously with higher BCMSD values than clean episodes. $eBCMSD_{AAC-AE33}$ and $rBCMSD_{DMA-SP2}$ were both integrated from 200 nm to 720 nm, which was the D_p range of measurement for DMA – SP2, and the results were denoted as $m_{eBC,bulk,AAC-AE33,par=200-720}$ and $m_{rBC,bulk,DMA-SP2,200-720}$, respectively. As shown in Fig. 2a, $m_{eBC,bulk,AAC-AE33,200-720,par}$ compared well with $m_{rBC,bulk,DMA-SP2,200-720}$ with determination coefficient (R^2), slope (b_1), and intercept (b_0) of 0.8 (accurate to one decimal place), 1.0 and $0.1 \mu g m^{-3}$ (Fig. S2a), R^2 of 0.8 and b_1 of 1.0 indicating indicated the proposed method was capable of capturing the variation of $m_{BC,bulk}$. The mean $m_{eBC,bulk,AAC-AE33,par=200-720}$ and $m_{rBC,bulk,DMA-SP2,200-720}$ were $0.7 \pm 0.4 \mu g m^{-3}$ and $0.6 \pm 0.3 \mu g m^{-3}$, indicating $m_{eBC,bulk,AAC-AE33,par=200-720}$ was overall $0.1 \mu g m^{-3}$ higher than $m_{rBC,bulk,DMA-SP2,200-720}$, consistent with b_0 of $0.1 \mu g m^{-3}$. The reason for overall discrepancy of $0.1 \mu g m^{-3}$ in $m_{BC,bulk,200-720}$ might be that DMA – SP2 could not detect rBC with D_c less than about 100 nm (Zhao et al., 2020a), resulting in an underestimated $m_{rBC,bulk,DMA-SP2,200-720}$. $eBCMSD_{AAC-AE33}$ was also integrated from 200-720 nm to 1500 nm, which was the D_p range of measurement for that DMA – SP2 did not measure, and the result was denoted as $m_{eBC,bulk,AAC-AE33,720-1500}$. $m_{eBC,bulk,AAC-AE33,720-1500}$ was correlated to $m_{rBC,bulk,DMA-SP2,200-720}$ to study whether BCMSD ranging from 720 nm to 1500 nm was connected to that ranging from 200 nm to 720 nm, as shown in Fig. S2b. R^2 decreased to 0.72, b_1 and b_0 increased to 1.2 and $0.2 \mu g m^{-3}$ between $m_{eBC,bulk,AAC-AE33,720-1500}$ and $m_{rBC,bulk,DMA-SP2,200-720}$, indicating these two size ranges were not well related and both of them needed to be measured exclusively. Observation by transmission electron microscopy showed that these larger BC-containing particles could be coated with massive materials from secondary processes, or superaggregated BC with fractal BC structure (Wang et al., 2022). The mean $m_{eBC,bulk,AAC-AE33,720-1500}$ was $0.9-2 \pm 0.5-2 \mu g m^{-3}$, $-0.2 \mu g m^{-3}$ higher than $m_{rBC,bulk,AAC-AE33,par}$, indicating that DMA – SP2 overall underestimated $m_{BC,bulk}$ for $\sim 0.2 \mu g m^{-3}$ ($\sim 33\%$) in this field measurement considering that DMA – SP2 could not measure BCMSD larger than about 720 nm. The decrease in R^2 indicated the BCMSD of larger D_p contained more sophisticated structure. Therefore, it was highly necessary to measure BCMSD with wider D_p range for better estimation of $m_{BC,bulk}$ and deeper understanding of BC evolution in the atmosphere.

Figure 3 exhibited the mean $eBCMSD_{AAC-AE33}$ ($\overline{eBCMSD}_{AAC-AE33}$) and mean $rBCMSD_{DMA-SP2}$ ($\overline{rBCMSD}_{DMA-SP2}$) during the

field measurement. It could be seen that when D_p was less than about 300 nm, $\overline{eBCMSD}_{AAC-AE33}$ was higher than $\overline{rBCMSD}_{DMA-SP2}$. The higher $\overline{eBCMSD}_{AAC-AE33}$ may be due to particle diffusion at small D_p which was not well corrected by (7) and underestimated MAC. When D_p was greater than 300 nm and less than ~~about 700-720 nm~~, $\overline{eBCMSD}_{AAC-AE33}$ was overall consistent with $\overline{rBCMSD}_{DMA-SP2}$. When D_p was larger than ~~700-720 nm~~, where DMA – SP2 ~~could did~~ not measure, $\overline{eBCMSD}_{AAC-AE33}$ decreased with increasing D_p when D_p less than about 870 nm, and increased with increasing D_p when D_p was larger than 870 nm. In the study by Yu et al. (2010), three modes of BCMSD were identified: the mode peaked at about 400 nm, 1000 nm and 5000 nm, which were termed as condensation mode, droplet mode and coarse mode, respectively. Following the nomenclature proposed by Yu et al. (2010), the increasing (decreasing) $\overline{eBCMSD}_{AAC-AE33}$ with increasing D_p for D_p larger (less) than 870 nm signified the lower (upper) end of droplet mode (condensation mode). However, $\overline{rBCMSD}_{DMA-SP2}$ only identified condensation mode, which clearly highlighted the necessity to measure BCMSD of wider D_p range for better characterization of BCMSD. Both the proposed method and DMA – SP2 showed that the temporal variation of BCMSD, expressed as standard deviation (std) of BCMSD in Fig. 3, was as large as \overline{BCMSD} , reflecting the complex mechanism in the variability of BCMSD.

4 Uncertainty analysis

Uncertainty analysis was performed with respect to the MAC lookup table, transfer function inversion from $\sigma_{ab,binned}$ to $\sigma_{ab,size-resolved}$, f_{BC} and instrumental noise, respectively. The resulting uncertainty to $\overline{eBCMSD}_{AAC-AE33}$ was illustrated in Fig. 4 and to $m_{eBC,bulk,AAC-AE33,200-720}$ was shown in table 1. It could be seen from Fig. 4 that the boundary between condensation mode and droplet mode was distinct no matter how the uncertainty sources disturbed $\overline{eBCMSD}_{AAC-AE33}$.

4.1 Uncertainty from mass absorption cross-section

According to Zhao et al. (2021b), the variation in refractive index (RI) dominated the uncertainty of the MAC lookup table. Therefore, the uncertainty from the MAC lookup table was analyzed with respect to RI. The real part of RI (Re[RI]) was reported to vary from 1.5 to 2.0 in general (Liu et al., 2018) and the imaginary part of RI (Im[RI]) ranged from 0.5 to 1.1 commonly (Bond and Bergstrom, 2006). Hence, Re[RI] (Im[RI]) was changed from 1.5 (0.5) to 2.0 (1.1) with step increase of 0.01, the resulting mean MAC (\overline{MAC}) was the MAC lookup table used in this study (Fig. S3a) and the resulting std divided by the \overline{MAC} was considered as the uncertainty of the MAC lookup table (Fig. S3b). As shown in Fig. ~~S2bS3b~~, when D_c was larger than about 400 nm, the uncertainty was less than 10% and influenced by both D_p and D_c . However, when D_c was less than 400 nm, the uncertainty increased rapidly with decreasing D_c and was dominated by D_c . The uncertainty increased to larger than 23 % when D_c was less than about 100 nm. When D_p was less than about 300 nm, the uncertainty varied from 14% to 24% with a mean value of 22 %, indicating large uncertainty in $\overline{eBCMSD}_{AAC-AE33}$ for D_p less than 300 nm.

The MAC lookup table was replaced with original \overline{MAC} minus its std (-stdMAC) and plus its std (+stdMAC). The resulting MAC lookup tables were taken into the method proposed by Zhao et al. (2021b), and applied to the entire measurement period to study the influence of MAC variation on the $\overline{eBCMSD}_{AAC-AE33}$. $\overline{eBCMSD}_{AAC-AE33}$ and mean $\overline{eBCMSD}_{AAC-AE33}$ ~~of-after~~ \pm stdMAC were shown in Fig. 4a. The uncertainty increased with decreasing D_p , and reached to maximum when D_p was less than 300

nm, indicating the $eBCMSD_{AAC-AE33}$ for D_p less than 300 nm might potentially have nonnegligible uncertainty. The uncertainty in $m_{eBC,bulk,AAC-AE33,200-720}$ was from -20 % (+stdMAC) to +28 % (-stdMAC), which was the largest among the four uncertainty sources, as shown in Table 1.

4.2 Uncertainty from the transfer function inversion

As stated in Sect. 2.4.1, correction for particle loss and spectral broadening was required when $\sigma_{ab,binned}$ was converted to $\sigma_{ab,size-resolved}$. λ_Ω was defined to correct particle loss where $\lambda_\Omega = 0$ ($\lambda_\Omega = 1$) stood for total (no) particle loss. The relationships between λ_Ω and D_p as well as Q_{sample} , as shown in Fig. S4a, were well developed (Karlsson and Martinsson, 2003) and consistent with experimental data of AAC (Johnson et al., 2018). Q_{sample} used in this study was 3.0 L min⁻¹. Q_{sample} was changed from -30 % (2.1 L min⁻¹) to +30 % (3.9 L min⁻¹), and the resulting λ_Ω was used to study the fluctuation of Q_{sample} on λ_Ω . As shown in Fig. S4a, the variation of λ_Ω was less than 0.5 %, which was negligible.

Spectral broadening was caused by small-size particle diffusion as well as fluctuation-disturbance of sheath flow due to complicated rotation fluid dynamics inside AAC and described by μ_Ω where $\mu_\Omega < 1$ ($\mu_\Omega = 1$) was for (no) broadening. μ_Ω was parameterized because of the complicated fluid dynamics and its interaction with particles. Johnson et al. (2018) found that behavior of μ_Ω with respect to D_p ($\mu_\Omega(D_p)$) depended on both Q_{sheath} and Q_{sample} , and parameterized $\mu_\Omega(D_p)$ (Fig. S4b) based on two case studies of (Q_{sheath} , Q_{sample}), namely (3 L min⁻¹, 0.3 L min⁻¹) and (15 L min⁻¹, 1.5 L min⁻¹) parameterized μ_Ω based on $Re = 10$ (Fig. S4b):

$$\mu_{\Omega,Johnson}(D_p) = 0.318 \cdot D_p^{0.0946} \quad (15)$$

However, (Q_{sheath} , Q_{sample}) Re was (7.5 L min⁻¹, 3 L min⁻¹) about 2.5 in this study, which might lead to uncertainty if $\mu_{\Omega,Johnson}(D_p)$ was directly used in this study. $\mu_{\Omega,Johnson}(D_p)$ was varied from -23 % to +30 % to study the impact of μ_Ω on $eBCMSD_{AAC-AE33}$. The reason for the lower limit of μ_Ω set as -23 % rather than -30 % was that $eBCMSD_{AAC-AE33}$ was negative when μ_Ω was less than -23 %. The resulting influence on the $eBCMSD_{AAC-AE33}$ was shown in Fig. 4b. The uncertainty of μ_Ω did not exhibit a significant size dependence. Lower μ_Ω led to lower $eBCMSD_{AAC-AE33}$, and vice versa. It should be noted that the uncertainty difference in the $m_{eBC,bulk,AAC-AE33,200-720}$ was from -1 % (-23% of $\mu_{\Omega,Johnson}$) to +21% (+30% of $\mu_{\Omega,Johnson}$), implying systematic overestimation of $m_{eBC,bulk,AAC-AE33,200-720}$. Therefore, $\mu_\Omega(D_p) = 77\% \mu_{\Omega,Johnson}(D_p)$ was used in this study was replaced with -23% of its original value in this work to offset the bias due to the incomplete μ_Ω parameterization. The reason for the lower limit of μ_Ω set as -23 % rather than -30 % was that $eBCMSD_{AAC-AE33}$ was negative invalid mathematically when μ_Ω was less than -23 % under setting of (Q_{sheath} , Q_{sample}) used in this study. It should be pointed out that AAC - AE33 could still determine valid $eBCMSD$ under the condition of $\mu_\Omega(D_p) < 77\% \mu_{\Omega,Johnson}(D_p)$ by increasing Q_{sheath} . Q_{sheath} was not changed in this study because desired $\mu_\Omega(D_p)$ parameterization was found at $\mu_\Omega(D_p) = 77\% \mu_{\Omega,Johnson}(D_p)$.

$\sigma_{ab,size-resolved}$ (Fig. S5b) was integrated and the result, denoted as $\sigma_{ab,bulk,calc}$ was compared to $\sigma_{ab,bulk}$. As shown in Fig. S5a, $\sigma_{ab,bulk,calc}$ was consistent with $\sigma_{ab,bulk}$. R^2 , b_1 and b_0 between $\sigma_{ab,bulk,calc}$ and $\sigma_{ab,bulk}$ was 0.9, 1.1, and 0.5 Mm⁻¹ (Fig. S6), respectively, which validated conversion from $\sigma_{ab,binned}$ to $\sigma_{ab,size-resolved}$.

带格式的: 字体: 倾斜

4.3 Uncertainty from number fraction of BC-containing particle

BC-containing aerosol particles had complicated mixing states. Even for internally-mixed particles with same D_p , the internal BC cores might have different D_c , which could not be resolved by AAC – AE33. Field measurement (Liu et al., 2010) revealed that f_{BC} varied with time, D_c and D_p . This complexity was simplified to a parameterized fixed value of f_{BC} in this study. A fixed f_{BC} implied that only one D_c value corresponded to a given D_p and the size-resolved number concentration of BC-containing particle was determined by $N_{\text{size-resolved}}$ times f_{BC} . Zhao et al. (2021b) used f_{BC} value of 0.17 based on SP2 measurement. However, SP2-derived f_{BC} could not represent the bulk f_{BC} over the whole particle size spectrum due to the detection limit of SP2. And different regions might have different f_{BC} . In this study, f_{BC} was varied and the resulting $m_{eBC, \text{bulk}, \text{AAC-AE33}, \text{pH} \sim 200-720}$ was compared with $m_{fBC, \text{bulk}, \text{DMA-SP2}, 200-720}$. f_{BC} was set as 0.35 in this study because b_1 was 1.0 between $m_{eBC, \text{bulk}, \text{AAC-AE33}, \text{pH} \sim 200-720}$ and $m_{fBC, \text{bulk}, \text{DMA-SP2}, 200-720}$ when f_{BC} was 0.35.

f_{BC} was varied from 0.25 (– 30 % of 0.35) to 0.46 (+ 30 % of 0.35) to analyze the influence of f_{BC} on the $eBCMSD_{\text{AAC-AE33}}$, as shown in Fig. 4c. $eBCMSD_{\text{AAC-AE33}}$ was more influenced around 870 nm. The variation of f_{BC} led to uncertainty of ± 3 % in $m_{eBC, \text{bulk}, \text{AAC-AE33}, 200-720}$, indicating that simplification of f_{BC} was a minor uncertainty source compared to MAC and transfer function inversion.

4.4 Uncertainty from instrumental noise

The instrumental noise stemmed from the fluctuation of the light source and flow of AE33, which was reflected as fluctuation in I , I_0 and F , further leading to the fluctuation in ATN, σ_{ATN} and σ_{ab} . The instrumental noise was defined as the std of $\sigma_{\text{ab}, \text{binned}}$ and was shown in Fig. S7b. It could be seen that the instrumental noise did not exhibit significant dependence on D_p . Comparing Fig. S7a and Fig. S7b, the instrumental noise was irrelevant to the value of $\sigma_{\text{ab}, \text{binned}}$. Figure S7c illustrated that the instrumental noise was also not correlated to $\sigma_{\text{ab}, \text{bulk}}$ with R^2 , b_1 and b_0 of 0.0, 0.0 and 0.1 Mm^{-1} , respectively, implying that the instrumental noise was not dependent on the pollution level.

The std of instrumental noise was added to (subtracted from) $\sigma_{\text{ab}, \text{binned}}$ and the derived $eBCMSD_{\text{AAC-AE33}}$ was used to study the influence of instrumental noise on $eBCMSD_{\text{AAC-AE33}}$. The mean result was shown in Fig. 4d. $eBCMSD_{\text{AAC-AE33}}$ larger than 1000 nm was more influenced by the instrumental noise than $eBCMSD_{\text{AAC-AE33}}$ smaller than 500 nm. $\sigma_{\text{ab}, \text{binned}}$ larger than 1000 nm was relatively small (about 0.3 Mm^{-1}) compared to $\sigma_{\text{ab}, \text{binned}}$ less than 870 nm (about 0.9 Mm^{-1}). The mean instrumental noise was 0.1 Mm^{-1} and exhibited no significant dependence on D_p . Therefore, $\sigma_{\text{ab}, \text{binned}}$ larger than 1000 nm was more affected by the instrumental noise, resulting in distinct variation in $eBCMSD_{\text{AAC-AE33}}$. Since the mass fraction of $m_{\text{BC}, \text{bulk}}$ was not dominated by BCMSD larger than 1000 nm in this study, the resulting uncertainty in $m_{eBC, \text{bulk}, \text{AAC-AE33}, 200-720}$ was not obvious, which varied from – 2 % to – 1 %, also minor compared to MAC and transfer function inversion.

5 Conclusions Summary

Knowledge of bulk black carbon (BC) characteristics, such as bulk BC mass concentration ($m_{\text{BC}, \text{bulk}}$), was very limited-limiting for deeper understanding the influence of BC on radiation and health. BC mass size distribution (BCMSD) was one of the BC

314 microphysical characteristics that could indicate emission source, reflect atmospheric aging and effectively reduce uncertainty
315 related to BC radiative effect. However, current BCMSD measurement ranging from upper micron to larger than 1 μm was
316 insufficient in time resolution and sophisticated for routine measurement. In this study, a new method to determine equivalent
317 BCMSD (eBCMSD) was proposed characterized by wide size range of measurement up to 1.5 μm , high time resolution up to 1
318 hour and convenience for extensive measurement. The eBCMSD was retrieved by size-resolved absorption coefficient ($\sigma_{\text{ab,size-resolved}}$)
319 measured by an aerodynamic aerosol classifier in tandem with an aethalometer model AE33 (AAC – AE33), denoted as
320 eBCMSD_{AAC-AE33}. Size-resolved number concentration ($N_{\text{size-resolved}}$) was measured concurrently by scanning mobility particle sizer
321 (SMPS) and an aerodynamic particle sizer (APS) to model the influence of size on mass absorption cross-section (MAC).

322 The proposed method was applied to a field measurement in Yangtze River Delta and validated by comparing the refractory
323 BCMSD (rBCMSD) with that measured by an differential mobility analyzer in tandem with a single-particle soot photometer (DMA
324 – SP2), denoted as rBCMSD_{DMA-SP2}. The results showed that for particle diameter (D_p) less than 300 nm, eBCMSD_{AAC-AE33} was
325 higher than rBCMSD_{DMA-SP2}, which might be caused by underestimated MAC by the method proposed by Zhao et al. (2021b) or
326 incomplete parameterization of spectral broadening of AAC. eBCMSD_{AAC-AE33} was consistent with rBCMSD_{DMA-SP2} for D_p larger
327 than 300 nm. $m_{\text{BC,bulk}}$ integrated over the size range that AAC – AE33 and DMA – SP2 both measured (200 nm – 720 nm), denoted
328 as $m_{\text{eBC,bulk,AAC-AE33,part-200-720}}$ and $m_{\text{rBC,bulk,DMA-SP2,200-720}}$, compared well with each other with determination coefficient (R^2), slope
329 (b_1), and intercept (b_0) of 0.8, 1.0 and 0.1 $\mu\text{g m}^{-3}$, respectively. However, DMA – SP2 could did not measure D_p larger than 700 nm,
330 leading to 0.2 $\mu\text{g m}^{-3}$ (33 %) underestimation of $m_{\text{BC,bulk}}$, highlighting the necessity to measure BCMSD with a wider size range.

331 Uncertainty analysis was performed with respect to MAC, transfer function inversion, number fraction of BC-containing particle
332 (f_{BC}) and instrumental noise. MAC was the largest uncertainty source, leading to significant uncertainty for D_p less than 300 nm and
333 about 24% uncertainty in $m_{\text{eBC,bulk,AAC-AE33,200-720}}$. Transfer function inversion was the second largest uncertainty source, which was
334 induced by incomplete parameterization of spectral broadening. The uncertainty in transfer function inversion led to systematic
335 overestimation of $m_{\text{eBC,bulk,AAC-AE33,200-720}}$, which was corrected in this study. Both f_{BC} and instrumental noise were minor uncertainty
336 sources and one order of magnitude less than MAC and transfer function inversion. f_{BC} was simplification of complicated BC mixing
337 states, leading to relatively big uncertainty in eBCMSD at 870 nm, around the boundary between condensation mode and droplet
338 mode. The eBCMSD for D_p larger than 1000 nm was more sensitive to instrumental noise.

339 ~~This study proposed a new method to determine BCMSD based on widespread filter-based measurement. The proposed method
340 was validated by well-designed field measurement and thorough uncertainty analysis, highlighting the necessity to measure BCMSD
341 with a wider size coverage for a more complete characterization of BCMSD. The new method provided a high time-resolution,
342 wide size coverage, convenient and cost-effective solution for BCMSD measurement. Hence, the proposed method had great
343 potential for widespread BCMSD measurement and was expected to promote the research of BC radiative effect, source
344 apportionment and atmospheric aging.~~

346 **Data availability**

347 The measurement data involved in this study are available upon request to the authors.

348 **Author contributions**

349 CZ determined the main goal of this study. WZ and GZ designed the methods. WZ carried them out and prepared the paper with
350 contributions from all co-authors.

351 **Competing interests**

352 The authors declare that they have no conflict of interest.

353 **References**

- 354 Bond, T. C.: Spectral dependence of visible light absorption by carbonaceous particles emitted from coal combustion, *Geophys. Res. Res.*
355 *Lett.*, 28, 4075-4078, 10.1029/2001gl013652, 2001.
- 356 Bond, T. C., Streets, D. G., Yarber, K. F., Nelson, S. M., Woo, J. H., and Klimont, Z.: A technology-based global inventory of black
357 and organic carbon emissions from combustion, *J. Geophys. Res.-Atmos.*, 109, 43, 10.1029/2003jd003697, 2004.
- 358 Bond, T. C., and Bergstrom, R. W.: Light absorption by carbonaceous particles: An investigative review, *Aerosol Science and*
359 *Technology*, 40, 27-67, 10.1080/02786820500421521, 2006.
- 360 Bond, T. C., Doherty, S. J., Fahey, D. W., Forster, P. M., Bernsten, T., DeAngelo, B. J., Flanner, M. G., Ghan, S., Karcher, B., Koch,
361 D., Kinne, S., Kondo, Y., Quinn, P. K., Sarofim, M. C., Schultz, M. G., Schulz, M., Venkataraman, C., Zhang, H., Zhang, S., Bellouin,
362 N., Guttikunda, S. K., Hopke, P. K., Jacobson, M. Z., Kaiser, J. W., Klimont, Z., Lohmann, U., Schwarz, J. P., Shindell, D., Storelvmo,
363 T., Warren, S. G., and Zender, C. S.: Bounding the role of black carbon in the climate system: A scientific assessment, *J. Geophys.*
364 *Res.-Atmos.*, 118, 5380-5552, 10.1002/jgrd.50171, 2013.
- 365 Castagna, J., Calvello, M., Esposito, F., and Pavese, G.: Analysis of equivalent black carbon multi-year data at an oil pre-treatment
366 plant: Integration with satellite data to identify black carbon transboundary sources, *Remote Sens. Environ.*, 235, 10,
367 10.1016/j.rse.2019.111429, 2019.
- 368 Chow, J. C., Watson, J. G., Crow, D., Lowenthal, D. H., and Merrifield, T.: Comparison of IMPROVE and NIOSH Carbon
369 Measurements, *Aerosol Science and Technology*, 34, 23-34, 10.1080/02786820119073, 2001.
- 370 DeCarlo, P. F., Slowik, J. G., Worsnop, D. R., Davidovits, P., and Jimenez, J. L.: Particle morphology and density characterization
371 by combined mobility and aerodynamic diameter measurements. Part 1: Theory (vol 38, pg 1185, 2004), *Aerosol Science and*
372 *Technology*, 39, 184-184, 10.1080/02786820590928897, 2005.
- 373 Drinovec, L., Mocnik, G., Zotter, P., Prevot, A. S. H., Ruckstuhl, C., Coz, E., Rupakheti, M., Sciare, J., Muller, T., Wiedensohler,
374 A., and Hansen, A. D. A.: The "dual-spot" Aethalometer: an improved measurement of aerosol black carbon with real-time loading
375 compensation, *Atmospheric Measurement Techniques*, 8, 1965-1979, 10.5194/amt-8-1965-2015, 2015.
- 376 Guo, Y. H.: Carbonaceous aerosol composition over northern China in spring 2012, *Environmental Science and Pollution Research*,
377 22, 10839-10849, 10.1007/s11356-015-4299-8, 2015.

带格式的: 行距: 1.5 倍行距

域代码已更改

带格式的: 字体: (默认) Times New Roman

378 Hansen, A. D. A., Rosen, H., and Novakov, T.: The aethalometer - an instrument for the real-time measurement of optical-absorption
379 by aerosol-particles, *Sci. Total Environ.*, 36, 191-196, 10.1016/0048-9697(84)90265-1, 1984.

380 Helin, A., Niemi, J. V., Virkkula, A., Pirjola, L., Teinila, K., Backman, J., Aurela, M., Saarikoski, S., Ronkko, T., Asmi, E., and
381 Timonen, H.: Characteristics and source apportionment of black carbon in the Helsinki metropolitan area, Finland, *Atmospheric*
382 *Environment*, 190, 87-98, 10.1016/j.atmosenv.2018.07.022, 2018.

383 Highwood, E. J., and Kinnarsley, R. P.: When smoke gets in our eyes: The multiple impacts of atmospheric black carbon on climate,
384 air quality and health, *Environment International*, 32, 560-566, 10.1016/j.envint.2005.12.003, 2006.

385 Johnson, T. J., Irwin, M., Symonds, J. P. R., Olfert, J. S., and Boies, A. M.: Measuring aerosol size distributions with the aerodynamic
386 aerosol classifier, *Aerosol Science and Technology*, 52, 655-665, 10.1080/02786826.2018.1440063, 2018.

387 Karlsson, M. N. A., and Martinsson, B. G.: Methods to measure and predict the transfer function size dependence of individual
388 DMAs, *Journal of Aerosol Science*, 34, 603-625, 10.1016/s0021-8502(03)00020-x, 2003.

389 Kim, J. H., Mulholland, G. W., Kukuck, S. R., and Pui, D. Y. H.: Slip correction measurements of certified PSL nanoparticles using
390 a nanometer differential mobility analyzer (nano-DMA) for Knudsen number from 0.5 to 83, *J. Res. Natl. Inst. Stand. Technol.*, 110,
391 31-54, 10.6028/jres.110.005, 2005.

392 Knutson, E. O., and Whitby, K. T.: Aerosol classification by electric mobility: apparatus, theory, and applications, *Journal of Aerosol*
393 *Science*, 6, 443-451, [https://doi.org/10.1016/0021-8502\(75\)90060-9](https://doi.org/10.1016/0021-8502(75)90060-9), 1975.

394 Liu, C., Chung, C. E., Yin, Y., and Schnaiter, M.: The absorption Angstrom exponent of black carbon: from numerical aspects,
395 *Atmospheric Chemistry and Physics*, 18, 6259-6273, 10.5194/acp-18-6259-2018, 2018.

396 Liu, D., Flynn, M., Gysel, M., Targino, A., Crawford, I., Bower, K., Choularton, T., Juranyi, Z., Steinbacher, M., Hüglin, C., Curtius,
397 J., Kampus, M., Petzold, A., Weingartner, E., Baltensperger, U., and Coe, H.: Single particle characterization of black carbon
398 aerosols at a tropospheric alpine site in Switzerland, *Atmospheric Chemistry and Physics*, 10, 7389-7407, 10.5194/acp-10-7389-
399 2010, 2010.

400 Matsui, H., Hamilton, D. S., and Mahowald, N. M.: Black carbon radiative effects highly sensitive to emitted particle size when
401 resolving mixing-state diversity, *Nature Communications*, 9, 10.1038/s41467-018-05635-1, 2018.

402 Moosmuller, H., Chakrabarty, R. K., and Arnott, W. P.: Aerosol light absorption and its measurement: A review, *Journal of*
403 *Quantitative Spectroscopy & Radiative Transfer*, 110, 844-878, 10.1016/j.jqsrt.2009.02.035, 2009.

404 Ning, Z., Chan, K. L., Wong, K. C., Westerdahl, D., Mocnik, G., Zhou, J. H., and Cheung, C. S.: Black carbon mass size distributions
405 of diesel exhaust and urban aerosols measured using differential mobility analyzer in tandem with Aethalometer, *Atmospheric*
406 *Environment*, 80, 31-40, 10.1016/j.atmosenv.2013.07.037, 2013.

407 Onasch, T. B., Trimborn, A., Fortner, E. C., Jayne, J. T., Kok, G. L., Williams, L. R., Davidovits, P., and Worsnop, D. R.: Soot
408 Particle Aerosol Mass Spectrometer: Development, Validation, and Initial Application, *Aerosol Science and Technology*, 46, 804-
409 817, 10.1080/02786826.2012.663948, 2012.

带格式的: 字体: (默认) Times New Roman

带格式的: 字体: (默认) Times New Roman

410 Petzold, A., Ogren, J. A., Fiebig, M., Laj, P., Li, S. M., Baltensperger, U., Holzer-Popp, T., Kinne, S., Pappalardo, G., Sugimoto, N.,
411 Wehrli, C., Wiedensohler, A., and Zhang, X. Y.: Recommendations for reporting "black carbon" measurements, *Atmospheric*
412 *Chemistry and Physics*, 13, 8365-8379, 10.5194/acp-13-8365-2013, 2013.

413 Ramachandran, S., and Rajesh, T. A.: Black carbon aerosol mass concentrations over Ahmedabad, an urban location in western
414 India: Comparison with urban sites in Asia, Europe, Canada, and the United States, *J. Geophys. Res.-Atmos.*, 112, 19,
415 10.1029/2006jd007488, 2007.

416 Ran, L., Deng, Z. Z., Wang, P. C., and Xia, X. A.: Black carbon and wavelength-dependent aerosol absorption in the North China
417 Plain based on two-year aethalometer measurements, *Atmospheric Environment*, 142, 132-144, 10.1016/j.atmosenv.2016.07.014,
418 2016.

419 Schwarz, J. P., Gao, R. S., Fahey, D. W., Thomson, D. S., Watts, L. A., Wilson, J. C., Reeves, J. M., Darbeheshti, M., Baumgardner,
420 D. G., Kok, G. L., Chung, S. H., Schulz, M., Hendricks, J., Lauer, A., Karcher, B., Slowik, J. G., Rosenlof, K. H., Thompson, T. L.,
421 Langford, A. O., Loewenstein, M., and Aikin, K. C.: Single-particle measurements of midlatitude black carbon and light-scattering
422 aerosols from the boundary layer to the lower stratosphere, *J. Geophys. Res.-Atmos.*, 111, 15, 10.1029/2006jd007076, 2006.

423 Schwarz, J. P., Spackman, J. R., Fahey, D. W., Gao, R. S., Lohmann, U., Stier, P., Watts, L. A., Thomson, D. S., Lack, D. A., Pfister,
424 L., Mahoney, M. J., Baumgardner, D., Wilson, J. C., and Reeves, J. M.: Coatings and their enhancement of black carbon light
425 absorption in the tropical atmosphere, *J. Geophys. Res.-Atmos.*, 113, 10, 10.1029/2007jd009042, 2008.

426 Soto-Garcia, L. L., Andreae, M. O., Andreae, T. W., Artaxo, P., Maenhaut, W., Kirchstetter, T., Novakov, T., Chow, J. C., and Mayol-
427 Bracero, O. L.: Evaluation of the carbon content of aerosols from the burning of biomass in the Brazilian Amazon using thermal,
428 optical and thermal-optical analysis methods, *Atmospheric Chemistry and Physics*, 11, 4425-4444, 10.5194/acp-11-4425-2011, 2011.

429 Tavakoli, F., and Olfert, J. S.: An Instrument for the Classification of Aerosols by Particle Relaxation Time: Theoretical Models of
430 the Aerodynamic Aerosol Classifier, *Aerosol Science and Technology*, 47, 916-926, 10.1080/02786826.2013.802761, 2013.

431 Taylor, J. W., Allan, J. D., Liu, D., Flynn, M., Weber, R., Zhang, X., Lefer, B. L., Grossberg, N., Flynn, J., and Coe, H.: Assessment
432 of the sensitivity of core / shell parameters derived using the single-particle soot photometer to density and refractive index, *Atmos.*
433 *Meas. Tech.*, 8, 1701-1718, 10.5194/amt-8-1701-2015, 2015.

434 Tunved, P., Cremer, R. S., Zieger, P., and Strom, J.: Using correlations between observed equivalent black carbon and aerosol size
435 distribution to derive size resolved BC mass concentration: a method applied on long-term observations performed at Zeppelin
436 station, Ny-Alesund, Svalbard, *Tellus Ser. B-Chem. Phys. Meteorol.*, 73, 1-17, 10.1080/16000889.2021.1933775, 2021.

437 Viidanoja, J., Kerminen, V.-M., and Hillamo, R.: Measuring the Size Distribution of Atmospheric Organic and Black Carbon Using
438 Impactor Sampling Coupled with Thermal Carbon Analysis: Method Development and Uncertainties, *Aerosol Science and*
439 *Technology*, 36, 607-616, 10.1080/02786820252883847, 2002.

440 Wang, J. D., Wang, S. X., Wang, J. P., Hua, Y., Liu, C., Cai, J., Xu, Q. C., Xu, X. T., Jiang, S. Y., Zheng, G. J., Jiang, J. K., Cai, R.
441 L., Zhou, W., Chen, G. Z., Jin, Y. Z., Zhang, Q., and Hao, J. M.: Significant Contribution of Coarse Black Carbon Particles to Light

442 Absorption in North China Plain, *Environ. Sci. Technol. Lett.*, 9, 134-139, 10.1021/acs.estlett.1c00953, 2022.

443 Yu, H., Wu, C., Wu, D., and Yu, J. Z.: Size distributions of elemental carbon and its contribution to light extinction in urban and
444 rural locations in the pearl river delta region, China, *Atmospheric Chemistry and Physics*, 10, 5107-5119, 10.5194/acp-10-5107-
445 2010, 2010.

446 Zhang, R. Y., Khalizov, A. F., Pagels, J., Zhang, D., Xue, H. X., and McMurry, P. H.: Variability in morphology, hygroscopicity, and
447 optical properties of soot aerosols during atmospheric processing, *Proceedings of the National Academy of Sciences of the United
448 States of America*, 105, 10291-10296, 10.1073/pnas.0804860105, 2008.

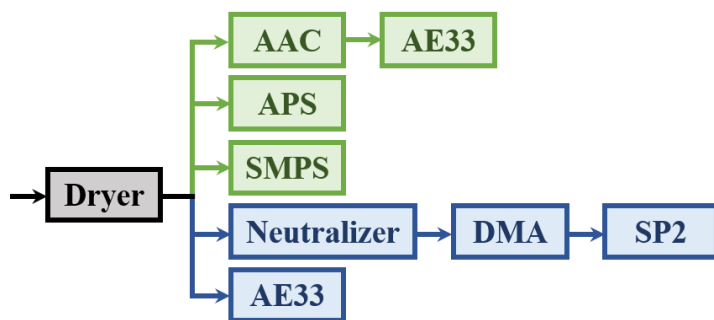
449 Zhao, G., Tao, J. C., Kuang, Y., Shen, C. Y., Yu, Y. L., and Zhao, C. S.: Role of black carbon mass size distribution in the direct
450 aerosol radiative forcing, *Atmospheric Chemistry and Physics*, 19, 13175-13188, 10.5194/acp-19-13175-2019, 2019.

451 Zhao, G., Shen, C. Y., and Zhao, C. S.: Technical note: Mismeasurement of the core-shell structure of black carbon-containing
452 ambient aerosols by SP2 measurements, *Atmospheric Environment*, 243, 10.1016/j.atmosenv.2020.117885, 2020a.

453 Zhao, G., Yu, Y., Tian, P., Li, J., Guo, S., and Zhao, C.: Evaluation and Correction of the Ambient Particle Spectral Light Absorption
454 Measured Using a Filter-based Aethalometer, *Aerosol and Air Quality Research*, 20, 10.4209/aaqr.2019.10.0500, 2020b.

455 Zhao, G., Tan, T. Y., Zhu, Y. S., Hu, M., and Zhao, C. S.: Method to quantify black carbon aerosol light absorption enhancement
456 with a mixing state index, *Atmospheric Chemistry and Physics*, 21, 18055-18063, 10.5194/acp-21-18055-2021, 2021a.

457 Zhao, W. L., Tan, W. S., Zhao, G., Shen, C. Y., Yu, Y. L., and Zhao, C. S.: Determination of equivalent black carbon mass
458 concentration from aerosol light absorption using variable mass absorption cross section, *Atmospheric Measurement Techniques*,
459 14, 1319-1331, 10.5194/amt-14-1319-2021, 2021b.



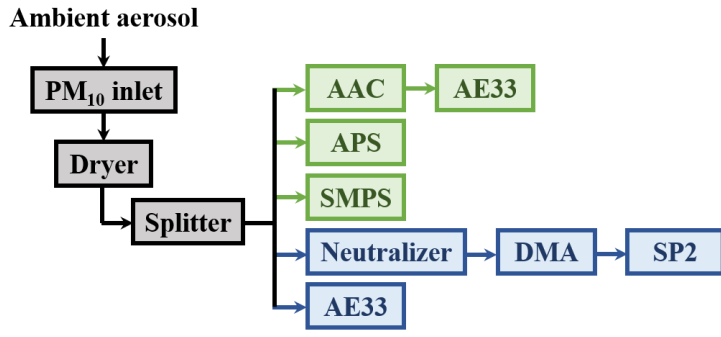
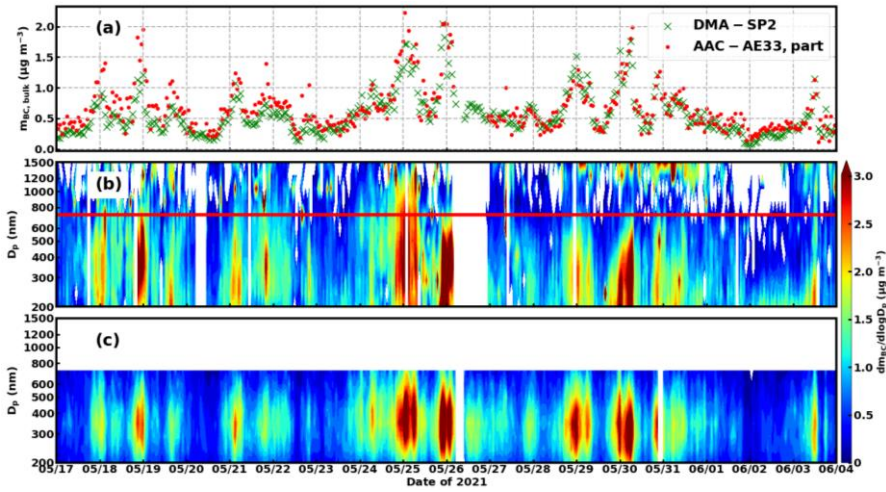
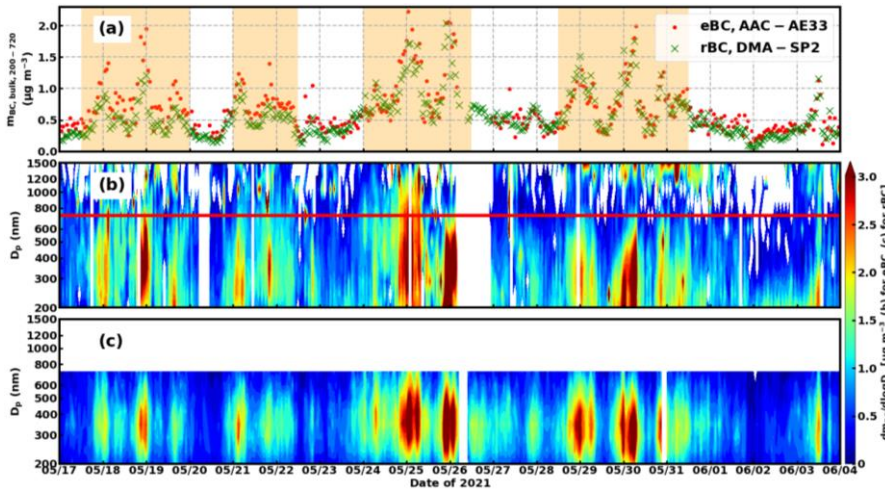
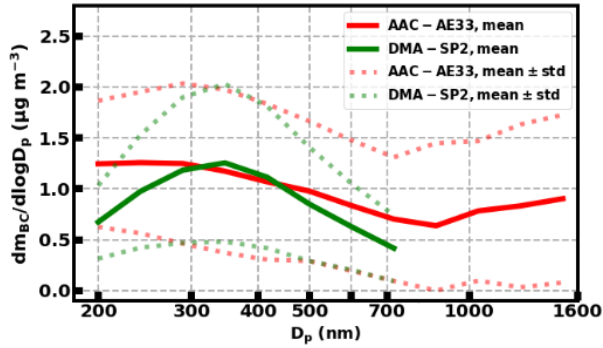


Figure 1: Schematic diagram of the measurement (green) and the validation (blue) setup.





467 Figure 2: Time series of (a) $m_{BC,bulk}$ from BCMSD integrated from 200 nm to 720 nm ($m_{BC,bulk,200-720}$) determined by the
 468 proposed method (red dot, denoted as “eBC, AAC – AE33”, part) and DMA – SP2 (green cross, denoted as “rBC, DMA –
 469 SP2”), BCMSD determined by (b) the proposed method (eBC) and (c) DMA – SP2 (rBC). The red line in (b) marked particle
 470 size of 720 nm. The pollution episodes were shaded with orange in (a).



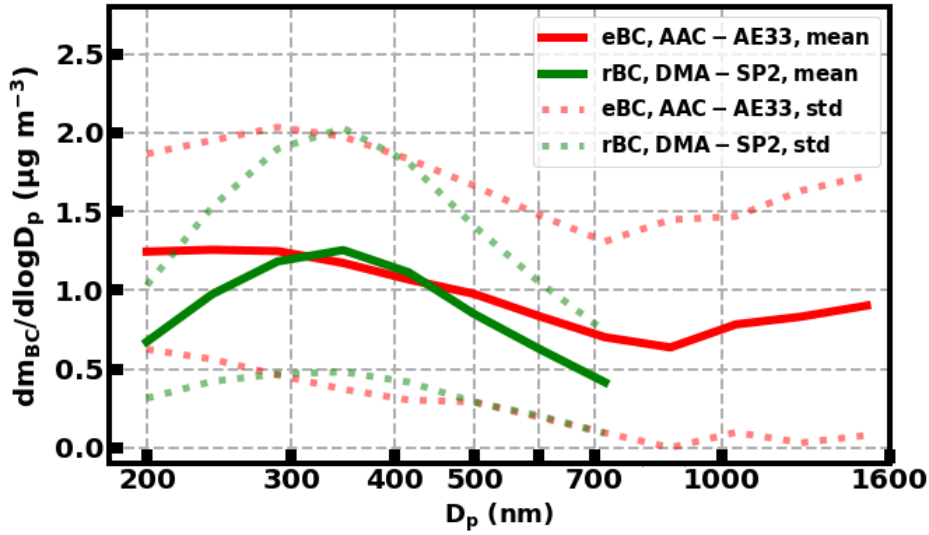
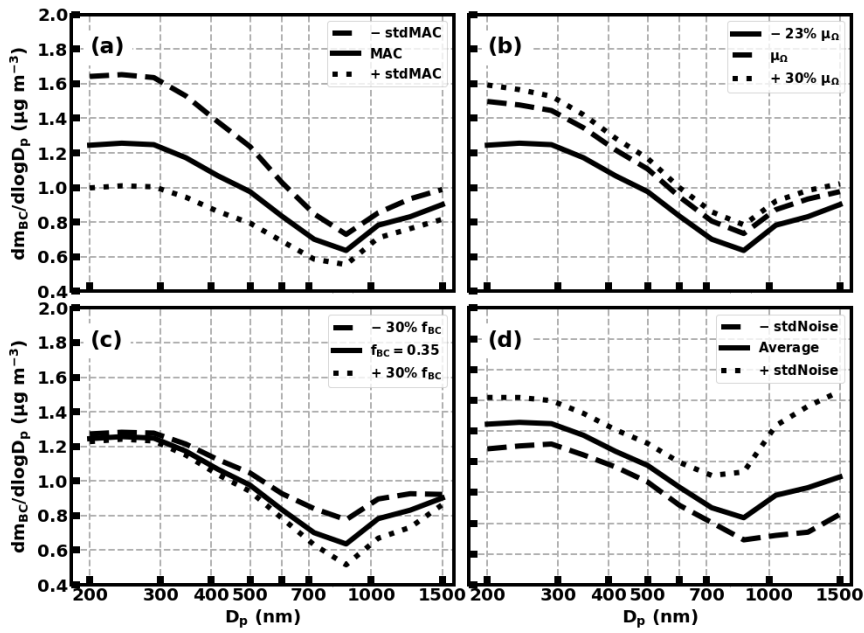


Figure 3: Mean and std of $\underline{e}BCMSD_{AAC-AE33}$ (green) and $\underline{r}BCMSD_{DMA-SP2}$ (red) during the measurement period. Mean BCMSD was denoted by the solid line. $\underline{Mean} \pm \underline{std}$ of BCMSD was denoted by the dotted line.



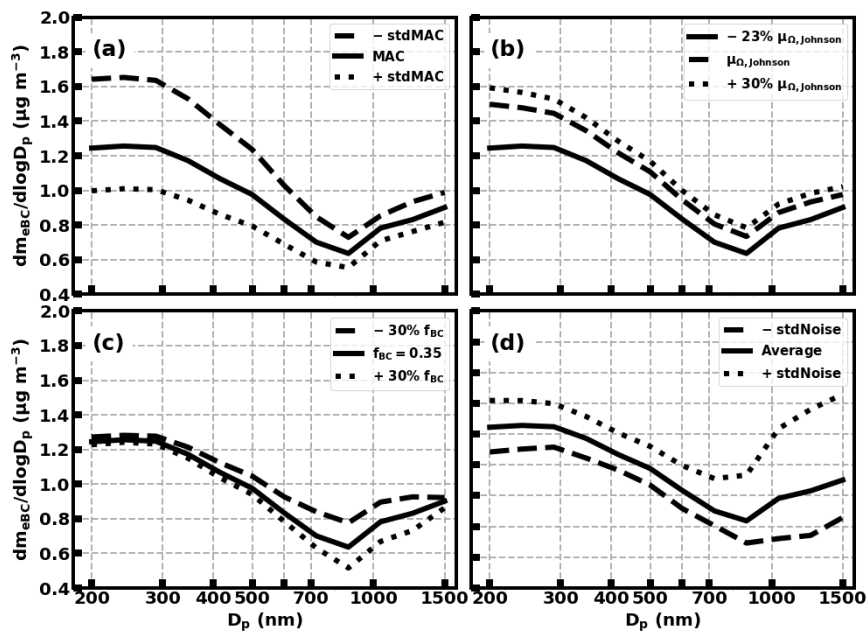


Figure 4: Uncertainty in $eBCMSD_{AAC-AE33}$ arising from (a) MAC lookup table, (b) transfer function inversion, (c) f_{BC} and (d) instrumental noise. The solid lines in each panel were the same and were the mean $eBCMSD_{AAC-AE33}$ during the measurement period. The dotted lines and dashed lines in each panel were mean $eBCMSD_{AAC-AE33} \pm$ standard deviation (std) calculated from (a) MAC + std of MAC and MAC - std of MAC, (b) default $\mu_{n,Johnson}$ and 1.3 times default $\mu_{n,Johnson}$, (c) f_{BC} of 35% times 0.7 and 1.3, (d) $eBCMSD_{AAC-AE33}$ + std of instrumental noise and - std of instrumental noise.

Table 1: The Uncertainty in the $m_{eBC,bulk,AAC-AE33,200-720} - m_{BC}$ resulted from MAC lookup table, transfer function inversion, f_{BC} and instrumental noise.

Uncertainty source	MAC	Transfer function inversion	f_{BC}	Instrumental noise
Uncertainty in $m_{eBC,bulk}$	-20% ~ +28%	-1% ~ +21%	-3% ~ +3%	-2% ~ -1%